Aerobrake Plasmadynamics: Macroscopic Effects

John V. Shebalin*
NASA Langley Research Center, Hampton, Virginia 23665

The flow around an aerobraking spacecraft (such as the aeroassist flight experiment re-entry vehicle) will contain a region of partially ionized gas, that is, a plasma. It is shown here by numerical simulation that macroscopic plasmadynamic effects (which are not included in standard aerothermodynamic simulations) will have a noticeable effect on the re-entry flowfield. In particular, there are thermoelectric phenomena that can have a major influence in flow dynamics at the front of an ionizing bowshock. These thermoelectric phenomena arise because of the presence of large density and temperature gradients at the front of a re-entry bowshock, and they include strong local magnetic fields, electric currents, and ohmic heating. One important result is the dramatic increase in temperature (over the case where plasma effects are neglected) at a re-entry shock front. The implication is that macroscopic plasmadynamic effects can no longer be neglected in aerothermodynamic simulations of hypersonic re-entry flowfields.

Introduction

THE plasma bowshock that surrounds a bluff hypersonic re-entry vehicle [i.e., an aerobraking spacecraft such as the aeroassist flight experiment (AFE) vehicle, which is illustrated in Fig. 1] results from shock-induced heating and ionization of the ambient atmospheric gas. Steep gradients in electron-number density and temperature across the shock transition layer have been computed[1] and are the source of potentially significant plasmadynamic effects: large magnetic fields, electric currents, and ohmic heating. Here, a relatively simple numerical experiment is used to demonstrate that such effects do, in fact, occur in situations that are characteristically similar to those encountered during the re-entry of an aerobraking spacecraft.

The inhomogeneous plasma environment caused by hypersonic re-entry is qualitatively similar to that produced by different mechanisms in other physical systems. For example, in high-power laser experiments, electromagnetic radiation incident on a material target creates a dense plasma that contains an ablation shock and its attendant large temperature and density gradients. In the first part of the 1970s, there was an intense effort[2-8] to understand the source of large (megagauss) local magnetic fields that were experimentally observed in these laser-produced plasmas.[9-10] The equations used in analytically modeling the plasmadynamic behavior were those corresponding to a two-temperature magnetohydrodynamic (MHD) model of a simple plasma.[2] Possible sources for the large magnetic fields seen included nonlinear magnetic processes,[2,5] radiation pressure,[4] and thermoelectric effects.[2,3,5,6,8] It was this latter source, the thermoelectric generation of magnetic fields and electric currents, which was recognized as predominant, particularly early in the evolution when local magnetic field strength was small.

The work presented here differs from this previous work concerning laser-induced plasma-shocks in that we need to include a neutral component. The basic procedure for doing this is well known[11,12] and will not be explicitly given here. The full set of equations are those pertinent to low frequency, macroscopic plasma motion; by "low frequency" it is meant that radiative processes are neglected. However, before looking in detail at the equations to be solved numerically, consider the following:

$$\partial_t(\rho u) + \nabla \cdot (\rho uu) = j \times B - \nabla p + F \tag{1}$$

$$\partial_t B = \nabla \times (u \times B - \eta j) + (k/e)\nabla T_e \times \ell n(n_e) \tag{2}$$

$$j = \mu_o^{-1} \nabla \times B \tag{3}$$

Here, $\partial_t \equiv \partial/\partial t$ and the various quantities in these equations are as follows:

ρ	= gas density, $kg \cdot m^{-3}$
u	= gas velocity, $m \cdot s^{-1}$
p	= gas pressure, $J \cdot m^{-3}$
F	= additional forces
B	= magnetic induction, T
j	= electric current density, $A \cdot m^{-2}$
n_e	= electron number density, m^{-3}
T_e	= electron temperature, K
μ_o	= $4\pi \times 10^{-7}$ H/m
η	= resistivity, $\Omega \cdot m$
(k/e)	= 0.862×10^{-4}, V/K
k	= Boltzmann's constant
e	= electronic charge

Equation (1) is the momentum equation (when F includes a dissipation term, it is the Navier-Stokes equation); Eq. (2) is the magnetic induction equation; and Eq. (3) states that the electric current is determined by the magnetic field. The last term on the right-hand side of Eq. (2) is the *thermoelectric* term. (The energy equation needed to complete this set will be added presently.)

Macroscopic plasmadynamic effects originate in Eq. (2) and affect the flow dynamics through the magnetic-force term ($j \times B$) in Eq. (1) and through heat-transfer terms in the energy or temperature equation. The first term on the right-hand side of Eq. (2) is the "standard" resistive MHD term; the second is the thermoelectric term. For a homogeneous plasma with subsonic flow, the gradients in density and temperature are often small enough so that the thermoelectric term can be legitimately neglected. In the inhomogeneous plasma associated with hypersonic flow, however, the ther-

Received June 26, 1989; revision received June 16, 1990; presented as Paper 90-1559 at the AIAA 21st Fluid Dynamics, Plasmadynamics, and Lasers Conference, Seattle, WA, June 18-20, 1990; second revision received Sept. 28, 1990; accepted for publication Oct. 7, 1990.

*Aerospace Technologist, Antenna and Microwave Research Branch. Member AIAA.

moelectric term may be more than an order of magnitude larger, and may be expected to dominate, as long as the gradients in electron temperature and number density are large and sufficiently nonparallel (almost-parallel gradients do not remain so, because of instability[5]). Presumably, the dominance of the thermoelectric term lasts until the growing magnetic field causes the other terms to grow sufficiently large, and all of the terms reach a dynamical balance (which is not necessarily a static equilibrium). Other terms may also be needed, such as a radiation pressure term in Eq. (1), or a magnetic pressure (Hall) term in Eq. (2), but this additional complexity will not be introduced here.

Equation (2), as it is written, requires that we determine the time-dependent electron number density and temperature fields in addition to the neutral density and temperature fields. Thus, a two-fluid model appears to be needed. However, the model can be reduced to a single-fluid model: 1) by assuming that the electron and neutral fluid temperatures are the same, and 2) through the use of the Saha equation. It is easily shown, by considering the exact form of the Saha equation,[13] that

$$\tfrac{1}{2}\nabla T \times \nabla \ell n(\rho) < \nabla T_e \times \nabla \ell n(n_e) < \nabla T \times \nabla \ell n(\rho) \qquad (4)$$

Assumptions 1 and 2 thus allow the creation of a single-fluid model [here we will use both the upper and lower limits of Eq. (4)].

Single-Fluid Equations

The simplest set of single-fluid equations are two-dimensional (in a one-dimensional model, the thermoelectric term is identically zero) with the magnetic field transverse to the dynamic plane, which will be taken to be the *x-y* plane (please see Fig. 1). The dynamic variables are functions of *x, y,* and the time *t*:

$$\lambda = \ell n\,(\rho/\rho_o), \quad \sigma = \ell n\,(T/T_o), \quad \boldsymbol{u} = u\hat{x} + v\hat{y}, \quad \boldsymbol{B} = B\hat{z} \qquad (5)$$

The natural logarithms of density and temperature are used since they may have any values between $-\infty$ and $+\infty$, while the density and temperature themselves must be positive definite, a requirement which sometimes causes numerical problems if the logarithmic form is not used.

The transport coefficients in the equations of motion are the fluid viscosity μ, electrical resistivity η, and thermal conductivity κ. These transport coefficients vary with temperature and density for a plasma; here they will be assumed to have the simple form:

$$\mu = \rho\nu_o, \qquad \eta = \eta_o, \qquad \kappa = \rho c_p \chi_o \qquad (6)$$

where the kinematic viscosity ν_o, resistivity η_o, specific heat at constant pressure c_p, and thermometric conductivity χ_o are all assumed constant, The adiabatic index $\gamma \equiv c_p/c_v$ will also be constant (c_p and c_v are the specific heats at constant pressure and volume, respectively; an "effective" γ will be determined later). The nondimensional equations of motion are then

Continuity:

$$\partial_t \lambda + \boldsymbol{u}\cdot\nabla\lambda = -\nabla\cdot\boldsymbol{u} \qquad (7)$$

Momentum:

$$\partial_t \boldsymbol{u} + \boldsymbol{u}\cdot\nabla\boldsymbol{u} = -c_1 e^{\sigma}\nabla(\sigma+\lambda) - (c_2/2)e^{-\lambda}\nabla B^2$$
$$+ c_3 e^{-\lambda}[\nabla\cdot(\mu''\nabla\boldsymbol{u}) + \partial_k(\mu''\nabla u_k) - \tfrac{2}{3}\nabla(\mu''\nabla\cdot\boldsymbol{u})]$$
$$\left\{ c_1 = \frac{kT_o}{M_{\mathrm{mol}}U_o^2}, \quad c_2 = \frac{B_o^2}{\mu_o\rho_o U_o^2}, \quad c_3 = \frac{\nu_o}{U_o L_o}, \quad \mu'' = e^{\lambda} \right\} \qquad (8)$$

Magnetic induction:

$$\partial_t B = \nabla\cdot(c_4\nabla B - B\boldsymbol{u}) + c_5 e^{\sigma}(\partial_x\sigma\partial_y\lambda - \partial_y\sigma\partial_x\lambda)$$
$$\left\{ c_4 = \frac{\eta_o}{\mu_o L_o U_o}, \qquad c_5 = \frac{kT_o}{eB_o U_o L_o} \times (\tfrac{1}{2} \text{ or } 1) \right\} \qquad (9)$$

Temperature:

$$\partial_t\sigma + \boldsymbol{u}\cdot\nabla\sigma = -c_6\nabla\cdot\boldsymbol{u} + c_7 e^{-\lambda-\sigma}\nabla\cdot(\kappa''\nabla e^{\sigma})$$
$$+ e^{-\lambda-\sigma}\left\{\frac{c_8\mu''}{2}\tau_{ij}\tau_{ij} + c_9(\nabla b)^2\right\}$$
$$+ c_{10}e^{-\lambda}(\partial_x B\partial_y\lambda - \partial_y B\partial_x\lambda) \qquad (10)$$
$$\left\{ \kappa'' = e^{\lambda}, \; c_6 = (\gamma-1), \quad c_7 = \frac{\chi_o}{L_o U_o}, \quad c_8 = \frac{c_3 c_6}{c_1}, \quad c_9 = \frac{c_2 c_4 c_6}{c_1}, \quad c_{10} = \frac{c_2 c_5 c_6}{c_1} \right\}$$

and

$$[\tfrac{1}{2}\,\tau_{ij}\tau_{ij} = \tfrac{2}{3}(\partial_x u - \partial_y v)^2 + \tfrac{2}{3}(\partial_x u)^2 + \tfrac{2}{3}(\partial_y v)^2 + (\partial_x v + \partial_y u)^2]$$

The dimensionless constants, c_i, $i = 1, \ldots, 10$, follow from the initial conditions, and will be given specific values shortly.

Again, the *thermoelectric* term is the last term on the right-hand side of Eq. (9), and it is this term that has the potential for generating large magnetic fields (and electric currents) Thermoelectric heat transfer is due to the last term on the right-hand side of Eq. (10), which is the well-known thermoelectric contribution to the heat flux,[14] and ohmic heating is due to the term with coefficient c_9.

Initial Conditions

The region of the re-entry bowshock whose characteristic values we use for our model is roughly a 10 × 10-cm square area ahead of the stagnation point, as shown in Fig. 1. We do not attempt to model all of the details of this region; instead, we initially model the shock as a finite-width pulse having velocity, temperature, and density values that correspond to those determined by aerothermodynamic simulations.[1] The initial flow thus consists of an upstream stream flow (having

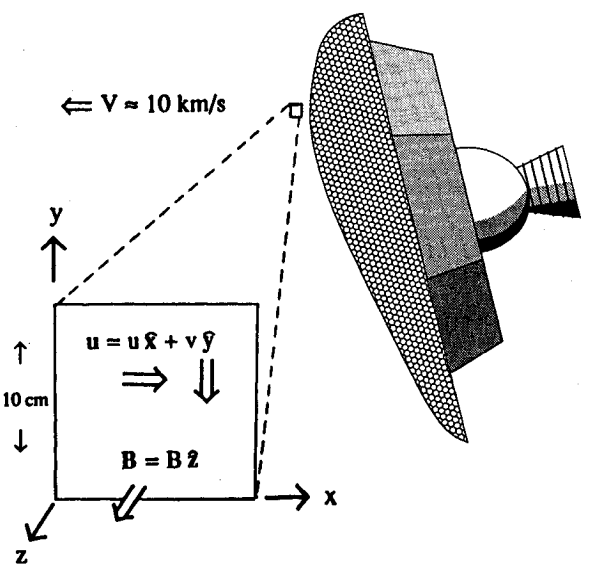

Fig. 1 Aeroassist flight experiment (AFE) vehicle (about 4 m across) is pictured with a two-dimensional region that corresponds to the computational geometry.

ambient values of velocity, temperature, density, and magnetic field) that makes a (shock-wave) transition into a finite width region, and then makes a (rarefaction-wave) transition into downstream flow (which again has the ambient values of velocity, temperature, density, and magnetic field). The values of the flow variables in the shock pulse itself will be connected to the ambient conditions by standard gasdynamic shock jump conditions[15] (the *Rankine-Hugoniot* conditions).

Since we wish to simulate flows similar to aerobrake re-entry conditions,[1] we choose upstream density and temperature corresponding to the AFE perigee altitude of about 80 km: 0.022 g/m^3 and 183 K, respectively[16]; for an aerobrake velocity of 8.65 km/s, this gives an upstream Mach number of $M_\infty = 32$ (with $\gamma_\infty = 1.4$). At this point we need an effective γ; since the temperature jump ratio for the AFE vehicle is estimated[1] to be about 100, and since we can invert the temperature jump relation, we get

$$\gamma = \gamma_{\text{eff}} \cong 1 + \frac{2}{M_\infty^2}\frac{T_{\text{shock}}}{T_\infty} = 1.20 \tag{11}$$

This gives values for velocity, density, and temperature within the shock of 0.794 km/s, 0.240 g/m^3, and 1.88×10^4 K, respectively. The effective Mach numbers are $M_{\text{eff}} = 34.6$ upstream and $M_{\text{eff}} = 0.313$ within the shock pulse.

Although it would be more accurate to use magnetogasdynamic jump conditions,[17] the initial magnetic field is small enough that there is only a slight difference between these and the gasdynamic ones. The magnetogasdynamic jump conditions are useful, however, in that they tell us that the ambient (transverse) magnetic field increases by the same proportion as the density: from 0.5 G upstream to 5.45 G within the shock. In order to determine the constants c_i, we will use the initial jump values and region size as being characteristic of the flow: $U_o = 0.794$ km/s; $T_o = 1.88 \times 10^4$ K; $\rho_o = 0.240$ g/m^3; $B_o = 5.45$ G; and $L_o = 10$ cm.

Next, in order to determine the constants c_i, the transport coefficients need to be assigned values. Since the region of interest is the shock transition region (i.e., the region between upstream and the initially flat part of the shock pulse), we need to find transport coefficient values pertinent to this region. Assuming that an average transition value of temperature is about 10^4 K, nominal values for the kinematic viscosity and resistivity can be estimated. Using known results for low-temperature plasmas,[18] along with the ratio[19] $\chi_o/\nu_o \approx (M_{\text{ion}}/m_e)^{1/2}$, we gain, as estimated values $\nu_o = 1$ m^2/s; $\eta_o \mu_o^{-1} = 265$ m^2/s; and $\chi_o = 210$ m^2/s. Here, M_{ion} is the heavy particle mass.

Using the characteristic flow values and transport coefficients given above, the various constants c_i can be determined (using the factor of ½ in c_5 initially):

$$c_1 = 8.49, \quad c_2 = 1.56 \times 10^{-3}, \quad c_3 = 1.26 \times 10^{-2}$$
$$c_4 = 3.34, \quad c_5 = 18.7, \quad c_6 = 0.2, \quad c_7 = 3.17$$
$$c_8 = 2.97 \times 10^{-5}, \quad c_9 = 1.23 \times 10^{-4}, \quad c_{10} = 6.87 \times 10^{-4} \tag{12}$$

Here, the ratio $c_5/c_4 = 6$ indicates that the evolution of the magnetic field is not dominated by resistivity, even though the "magnetic Reynolds number" $(c_4)^{-1}$ is small.

The initial values of the temperature, magnetic field, and velocity in the two-dimensional model space were one-dimensional, going from ambient upstream values, through a smooth front transition region, to shock values, through a smooth rear transition region, back to ambient values. The density, although it also had initially one-dimensional initial values everywhere else, had a curved (i.e., two-dimensional) smooth shock-wave transition region. The density shock transition region was designed so that the thermoelectric term in Eq. (9) would initially produce a maximum magnetic-field growth rate that was equivalent to the maximum that could be inferred from available aerothermodynamic shock-front numerical grid point values[20]; this was about 1000 T/s (1 T = 10^4 G). Although this may appear to be a rather large value, in reality, shock fronts may be expected to be much steeper than aerothermodynamic predictions (which are limited by using a relatively wide spacing at the shock front), so that magnetic field growth rates may have initially much larger values than even these predictions indicate.

The initial conditions used here thus represent an almost one-dimensional Mach 35 pulse, two-dimensionality occurring solely due to a curved density subshock front. In the numerical procedure (to be described in the next section), a grid of 128 points in the x direction by 128 points in the y direction was used. Freestream flow was initially in the x direction; the initial upstream region went from x-point 1 to x-point 26; the front transition region went from x-point 27 to x-point 44; the jump region went from x-point 45 to x-point 90; the rarefaction transition region went from x-point 91 to x-point 108; the ambient flow region behind the pulse went from x-point 109 to x-point 128. The transition of temperature and velocity from x-point 27 to x-point 44, and of density, temperature, and velocity from x-point 91 to x-point 108 was effected by the formula

$$F(x) = F_1 \cos^2(x - x_1) + F_2 \sin^2(x - x_2)$$
$$\left(x = n\frac{2\pi}{128}, \qquad x_i = n_i\frac{2\pi}{128}\right) \tag{13}$$

In the front (shock-wave) transition region, F_1 is the upstream value and F_2 is the jump value of T or u, and n runs from $n_1 = 26$ to $n_2 = 44$; In the rear (rarefaction) transition region, F_1 is the jump value and F_2 is the ambient value of ρ, T, or u, and n runs from $n_1 = 91$ to $n_2 = 108$. Within both transition regions, the magnetic field varies as (B_∞ is the ambient field of 0.5 G)

$$B(x) = B_\infty u_\infty / u(x) \tag{14}$$

In the front (shock-wave) transition region, the density transition varies exactly in the same manner as T and u in Eq. (13), except that n_1 and n_2 are determined by the formula

$$n_2(y) = 38 + 6\cos(y), \qquad n_1 = n_2 - 6$$
$$y = m\frac{2\pi}{128}, \qquad m = 0, 1, \ldots, 127 \tag{15}$$

The result of all this is shown in Fig. 2, where contours between the different subshock regions are given.

Numerical Method

The numerical technique used to simulate shock-front dynamics is a Fourier spectral method, whereby the partial differential Eqs. (8–10) are replaced by several thousand coupled ordinary differential equations, one for each of the independent Fourier coefficients. Quadratic nonlinear terms are evaluated by temporarily imbedding each of the two 128×128 Fourier coefficient grids in a 256×256 Fourier coefficient grid (the higher-order coefficients are all zero, and thus this is called *zero-padding*[21]), transforming each 256×256 Fourier grid to a 256×256 physical space grid, and multiplying these grids together, pointwise. Then, transforming the resultant 256×256 physical grid back to Fourier space, and reducing back to a 128×128 Fourier grid (thus there are only two 256×256 grids in the code), produces the nonaliased Fourier coefficients of the quadratic product. Although this may seem less elegant than other quadratic dealiasing procedures,[21] it has the advantage that it retains all $(128)^2$ independent sine and cosine coefficients and thereby maintains a 1-1 correspondence between Fourier-space grid points and physical-space

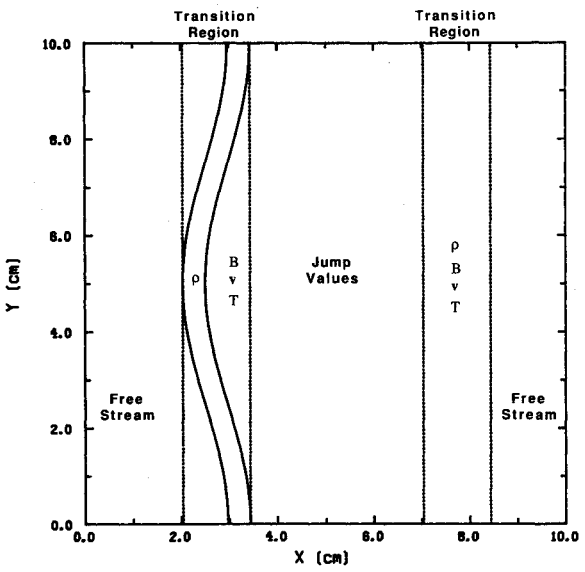

Fig. 2 Initial contours for runs N, P1, and P2. All initial variables are one-dimensional except for the density, whose transition from upstream to jump flow occurs across the indicated curved region. Initial values inside and outside the shock pulse are connected by standard (MHD or gas) Rankine-Hugoniot jump conditions.

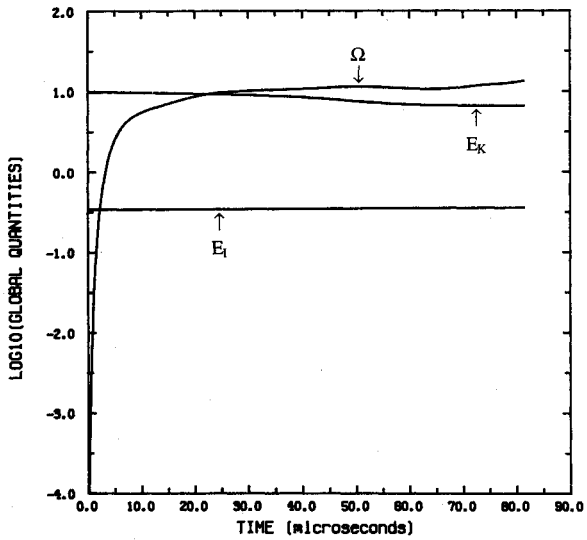

Fig. 3 Time histories of global kinetic (E_K) and internal (E_I) energies, and enstrophy (Ω) for run N (no plasmadynamic effects) are shown here. These quantities behaved very similarly for runs P1 and P2 (plasmadynamic effects included). (Here, $E_I/100$ appears.)

grid points. This is critical here, where we are concerned with the detailed development of physical-space flow structures, as opposed to studies of homogeneous turbulence,[22] where the object of primary importance is the Fourier spectrum itself, and physical space is merely a convenient mechanism for evaluating nonlinear terms (in which case the number of physical space grid points may be greater than the number of independent sine and cosine coefficients).

Although all quadratic nonlinearities are evaluated by the above dealiasing procedure, cubic and higher-order nonlinearities are not exactly dealiased when they are evaluated. Cubic nonlinearities are evaluated by taking two of the terms, performing the above quadratic evaluation procedure on them, and then performing the same procedure on the product of the result and the third term (this has been found to have some inherent aliasing error[23]). Exponential terms, such as $\exp(A)$, are evaluated by zero-padding the Fourier coefficients A to a 256×256 grid, transforming to physical space, directly forming $\exp(A)$, transforming this back to Fourier space, and truncating back to the 128×128 grid size. Since the evaluation of nonlinearities higher than quadratic has some inherent aliasing error, the overall effect is that we have a "pseudospectral," or "collocation" method, rather than a "fully spectral" method. However, since aliasing effects have never appeared to be a real problem in dissipative simulations, pseudospectral methods, in general, appear to be sufficiently robust for these simulations.

Time integration is accomplished using an explicit "partially corrected Adams-Bashforth scheme of order 3"[24] for the nondissipative terms in Eqs. (8–10), while the dissipative terms are handled implicitly. Also, a variable time-step size is used, as is necessary for compressible flow simulations.[25]

Numerical Results

The simulation was run on the Cray 2 computer at NASA Ames, with the CPU time per simulation time step being 5.4 s. Here, the results of three runs will be presented: Run N: 4800 time steps, with plasma effects "off," i.e., $c_2 = c_4 = c_5 = 0$ in Eq. (12); Run P1: 6000 time steps, with all plasma effects turned "on" and with the c_i as given in Eq. (12); Run P2: 6000 time steps, with all plasma effects turned "on" and with the c_i as given in Eq. (12) except that $c_5 = 37.4$. A number of other simulations were also run, but will not be explicitly presented here. Runs N, P1, and P2 should be sufficient to show the result of introducing plasma effects into gasdynamic simulations. Runs N, P1, and P2 all had identical initial conditions, except that run N began with (and maintained) a zero magnetic field.

To begin, consider the global averages given in Figs. 3 and 4 ("global" because they are determined by averaging over the whole computational domain):

$$E_K \equiv \frac{1}{2} N^{-2} \sum_x \boldsymbol{p}(x) \cdot \boldsymbol{u}(x), \qquad \boldsymbol{p}(x) = \rho(x)\boldsymbol{u}(x)$$

$$E_I \equiv \frac{c_1}{c_6} N^{-2} \sum_x \rho(x) T(x)$$

$$E_M \equiv \frac{1}{2} c_2 N^{-2} \sum_x |\boldsymbol{B}(x)|^2$$

$$\Omega \equiv \frac{1}{2} N^{-2} \sum_x |\omega(x)|^2 \qquad (\omega = \nabla \times \boldsymbol{u})$$

$$J \equiv \frac{1}{2} c_2 N^{-2} \sum_x |\boldsymbol{j}(x)|^2 \qquad (\boldsymbol{j} = \nabla \times \boldsymbol{B}) \tag{16}$$

Here, we are averaging over all gridpoints, and ω and $\boldsymbol{j}$ are the (nondimensional) vorticity, and current, respectively. Also, E_K is the kinetic energy, E_I is the internal energy, E_M is the magnetic energy, Ω is the enstrophy (mean squared vorticity), and J is a measure of mean squared current. $N(=128)$ is the number of grid points in one dimension.

Figure 3 shows the time histories of E_K, E_I, and Ω for run N (the same quantities in runs P1 and P2 had essentially the same behavior). We see that the mean square vorticity Ω grows relatively quickly over about the first 10 μs, and then levels off; also, E_K decays slightly from start to finish because we have a free shock, rather than one which is driven by a re-entry body. Figure 4 shows the time histories of E_M and J for runs P1 and P2, which grow relatively quickly for about the first 30 μs, and then level off. The pairs of curves for E_M and for J may be considered as bounds for global magnetic behavior in the two-dimensional model system under investigation.

Now, we will examine the flow variables of the three runs at approximately the same times into their evolution ($t \approx 70$ μs). In Figs. 5–8 are comparisons of the one nonplasma run (N) and the two plasma runs (P1 and P2). These comparisons are

effected through the use of "transverse" root-mean-square (rms) profiles: rms values of the various physical variables are calculated for all y values at each value of x, the variable in the direction of the mean flow. In Figs. 5 and 6, the transverse rms profiles of density and streamwise velocity, respectively, appear; the initial profile along with those of runs N and P2 are given (the profiles of run P1 are intermediate to those of runs P2 and N). In Fig. 7, the transverse rms temperature profiles for all three runs are given (along with the initial profile); this figure perhaps most dramatically shows the need for including plasmadynamic terms in aerothermodynamic simulations. In Fig. 8, the transverse rms vorticity profiles are given for runs N and P2 (run P1 is again intermediate to N and P2, and the initial vorticity was zero everywhere).

In Figs. 9–11, transverse rms profiles that pertain only to a plasma are given. These are the magnetic field (Fig. 9), current (Fig. 10), and net electric charge density (Fig. 11). The net charge density ρ_e is determined from $\epsilon_o \nabla \cdot \boldsymbol{E} = \rho_e$, where ϵ_o is the electric permittivity of free space. In order to get an appreciation of the magnitude of net charge density, the electric field may be approximated (for our single fluid model) by

$$\boldsymbol{E} = \eta \boldsymbol{j} - \boldsymbol{u} \times \boldsymbol{B} - (k/e)T \nabla \ell n \rho \qquad (17)$$

[When this is placed into Ampere's Law, $\partial_t \boldsymbol{B} = -\nabla \times \boldsymbol{E}$, we get Eq. (9).] Although the maximum rms net charge density of around 10^7 electric charges per cubic centimeter is exceedingly small when compared to the maximum expected[1] electron number density of about 10^{13} per cubic centimeter, it is large compared to the ambient ionospheric electron number density of about 10^3–10^5 per cubic centimeter. Since the net charge appears to be largest right at the shock front, it may noticeably affect microscopic dynamic processes there.

In addition, the high magnetic field and electric current levels indicated by Figs. 9 and 10 lead to some interesting possibilities. First, there is still time to include a simple magnetometer on the AFE; this would clearly indicate whether or not plasmadynamic processes were actually occurring. Second,

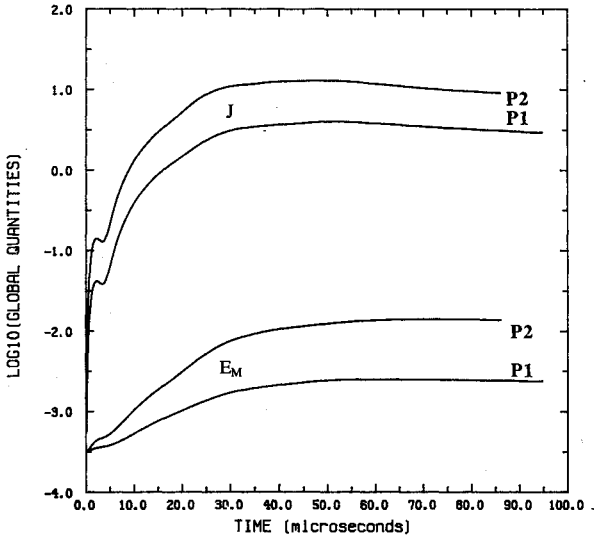

Fig. 4 Time histories of global magnetic energy (E_M) and mean square current (J) for runs P1 and P2 (the thermoelectric coefficient for P2 is twice that of P1). Runs P1 and P2 may be considered as rough lower and upper (mean square) bounds, respectively, on the possible plasmadynamic behavior in this two-dimensional model system.

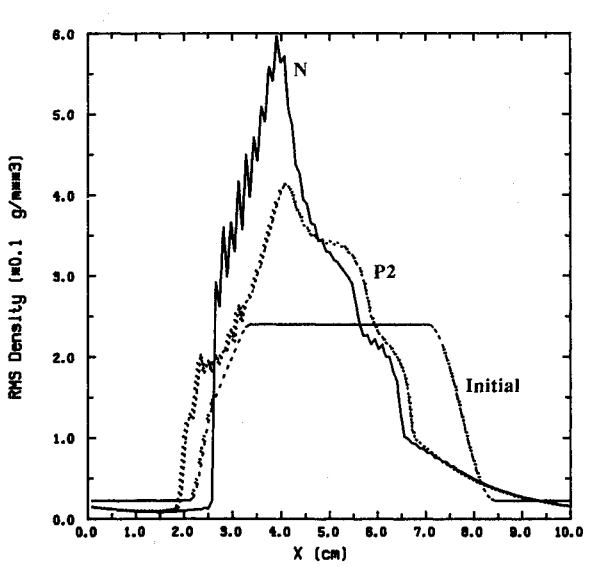

Fig. 5 Transverse rms mass density for runs N and P2 at $t \approx 70$ μs. The regular, pulse-shaped curve represents the initial conditions (ambient-to-jump-to-ambient values). Mean flow goes from left to right.

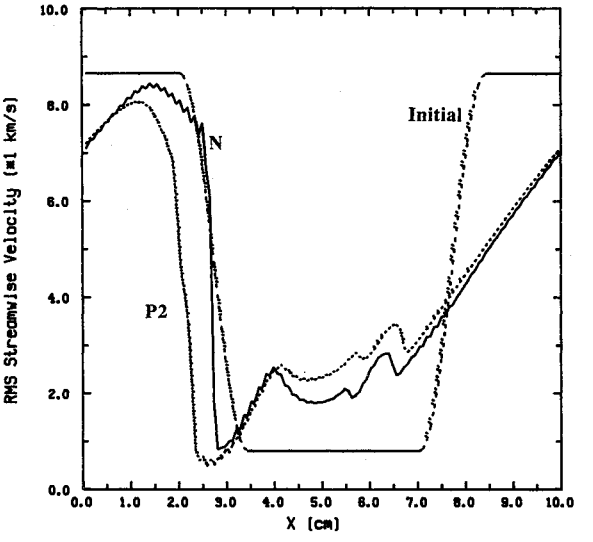

Fig. 6 Transverse rms velocity for runs N and P2 at $t \approx 70$ μs. The regular, pulse-shaped curve represents the initial conditions (ambient-to-jump-to-ambient values). Mean flow goes from left to right.

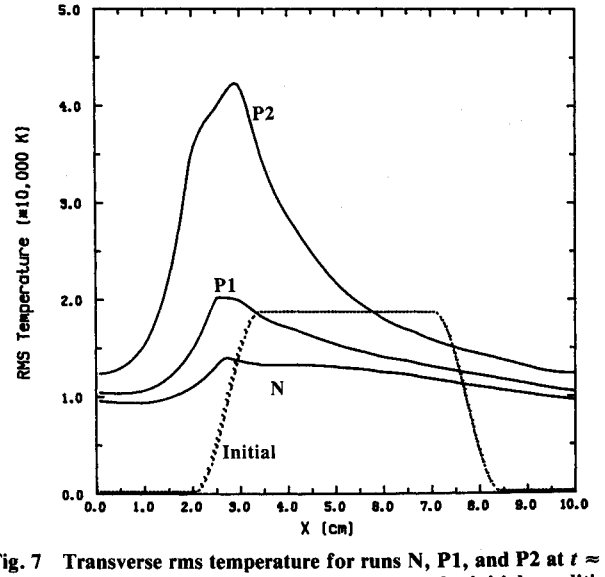

Fig. 7 Transverse rms temperature for runs N, P1, and P2 at $t \approx 70$ μs. The regular, pulse-shaped curve represents the initial conditions (ambient-to-jump-to-ambient values). Mean flow goes from left to right.

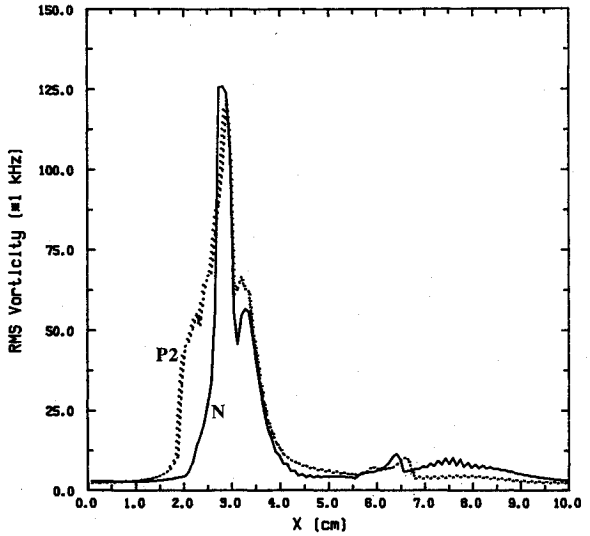

Fig. 8 Transverse rms vorticity for runs N and P2 at $t \approx 70$ μs. The regular, pulse-shaped curve represents the initial conditions (ambient-to-jump-to-ambient values). Mean flow goes from left to right.

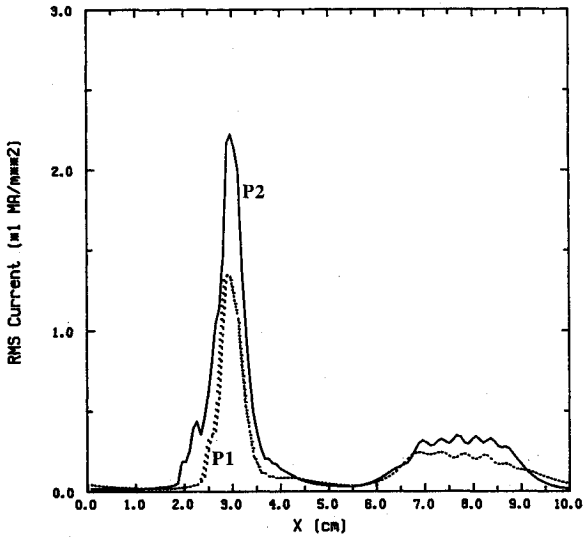

Fig. 10 Transverse rms current density for runs P1 and P2 at $t \approx 70$ μs. The regular, pulse-shaped curve represents the initial conditions (ambient-to-jump-to-ambient values). Mean flow goes from left to right.

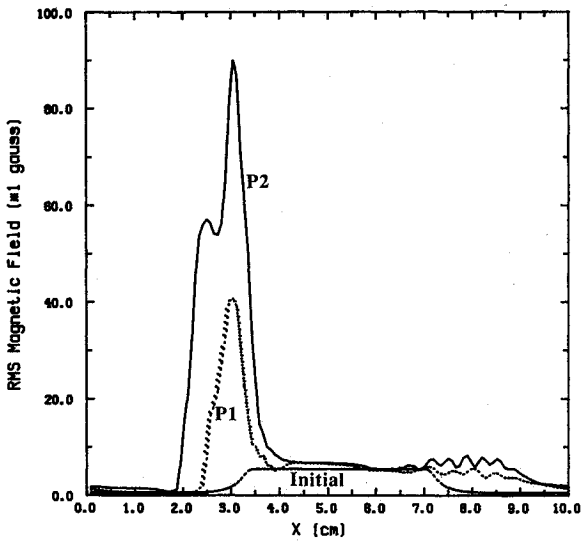

Fig. 9 Transverse rms magnetic field for runs P1 and P2 at $t \approx 70$ μs. The regular, pulse-shaped curve represents the initial conditions (ambient-to-jump-to-ambient values). Mean flow goes from left to right.

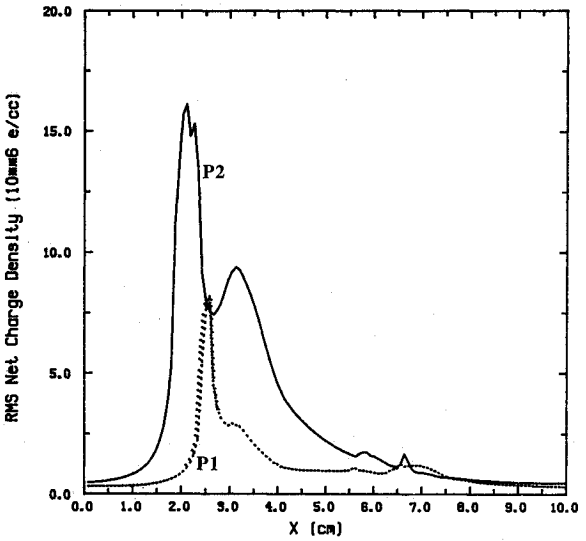

Fig. 11 Transverse rms net charge density for runs P1 and P2 at $t \approx 70$ μs. The regular, pulse-shaped curve represents the initial conditions (ambient-to-jump-to-ambient values). Mean flow goes from left to right.

high local electric current levels at a re-entry shock front may provide a means for manipulating the flowfield; this includes the possibility of using an electromagnet within an aerobraking vehicle to "magnetically" insulate the vehicle, and thereby augment presently used thermal-protection systems.

Discussion

Macroscopic plasmadynamic effects manifest themselves in the flow around an aerobraking re-entry vehicle in several ways. First, they broaden the shock front, as indicated in Figs. 5–8. Second, they raise the temperature dramatically, as Fig. 6 indicates (in comparison to the case where plasma effects are completely neglected). This large temperature increase must, in turn, cause a substantial increase in ionization and electron number density. This fact alone implies that aerothermodynamic predictions concerning electron number density are fundamentally incorrect; coupled with the admitted poor fit that aerothermodynamic predictions have with known experimental results for electron number density,[1] aerothermodynamics must be regarded as invalid when the hypersonic flowfields under consideration are sufficiently ionized (although it appears to work very well for un-ionized flows[1]).

In addition to the plasma effects considered here, which stem primarily from thermoelectric contributions to the local electric field, there are other terms that can be included in the flow equations. First, there is the "Hall," or magnetic force, term that is present in a more complete expression of the macroscopic electric field (also known as a "generalized Ohm's Law"; see p. 28 of Ref. 11):

$$E = \eta j - u \times B - \frac{k}{en_e} \nabla(n_e T_e) + \frac{j \times B}{en_e} \tag{18}$$

In Eq. (18), however, the simplifying assumptions that lead to Eqs. (4), (9), and (17) cannot be readily applied so as to reduce the last term in Eq. (18) (the Hall term) to a form suitable for single fluid modeling. Thus, a multispecies model is required for the case in which the magnetic field has increased significantly and the Hall term becomes important. Such multispecies models already exist,[1] however, and there appears to be no reason why they cannot be augmented so as to include those plasmadynamic terms that cannot be neglected.

Second, there are radiative terms that may also be important, particularly when high temperatures and ionization levels are reached. These terms were not included here, nor are they presently included in aerothermodynamic efforts.[1] It is, of course, imperative to critically evaluate radiative (or other potentially important) terms, at least qualitatively, in order to determine the validity of neglecting them or the necessity of incorporating them, with regard to whatever flow conditions are being modeled.

It must be repeated that the simulation described herein, the simplest one which has the possibility of exhibiting thermoelectric effects, is two-dimensional. Expanding the model (and vector fields $\boldsymbol{u}$ and $\boldsymbol{B}$) fully to three dimensions will allow the inclusion of additional effects, such as vortex stretching in Eq. (8) and $\boldsymbol{B} \cdot \nabla \boldsymbol{B}$ effects in Eq. (9), which do not occur in the present model. In going from two to three dimensions, however, we expect the generation of magnetic quantities to increase rather than decrease, for example, because well-known "antidynamo" theorems, which hold in two dimensions, do not hold in three dimensions.

Conclusion

In this work it has been shown that if plasmadynamic terms are included in the equations describing the motion of an ionized shock wave, then there are significant effects on the flow evolution. That these plasma effects are nonnegligible can be seen when two simulations, one with plasma effects "off" and the other with plasma effects "on," starting from identical initial conditions, are allowed to dynamically evolve: the run with plasma effects "on" has profile broadening and greatly increased temperature at the shock front. The root cause of these effects is a thermoelectric field that creates large electric currents and magnetic fields.

Furthermore, it appears that currently accepted aerothermodynamic approaches to the modeling of hypersonic plasma bowshocks are not valid: 1) because they do not match available experimental plasma profiles, and 2) because important terms are explicitly excluded. These approaches work well in modeling un-ionized flows and it may be expected that once all significant terms (plasma and radiative) are included, they will also work for ionized flows. Until then, however, aerothermodynamic predictions of such intrinsically plasma quantities as electron number density must be discounted.

Acknowledgments

I wish to thank Dr. Adam Drobot of SAIC and Professors David Montgomery, Bengt Sonnerup, and Professor Emeritus Arthur Kantrowitz of Dartmouth College for useful discussions.

References

[1]Gnoffo, P. A., "Code Calibration Program in Support of the Aeroassist Flight Experiment," *Journal of Spacecraft and Rockets,* Vol. 27, March-April 1990, pp. 131-141.

[2]Chase, J. B., LeBlanc, J. M., and Wilson, J. R., "Role of Spontaneous Magnetic Fields in a Laser-Created Deuterium Plasma," *Physics of Fluids,* Vol. 16, July 1973, pp. 1142-1148.

[3]Winsor, N. K., and Tidman, D. A., "Laser Target Model," *Physical Review Letters,* Vol, 31, 22 Oct. 1972, pp. 1044-1046.

[4]Stammper, J. A., and Tidman, D. A., "Magnetic Field Generation Due to Radiation Pressure in a Laser-Produced Plasma," *Physics of Fluids,* Vol. 16, Nov. 1973, pp. 2024-2025.

[5]Tidman, D. A., and Shanny, R. A., "Field-Generating Thermal Instability in Laser-Heated Plasmas," *Physics of Fluids,* Vol. 17, June 1974, pp. 1207-1210.

[6]Tidman, D. A., "Thermally Generated Magnetic Fields in Laser-Driven Compressions and Explosions," *Physics of Fluids,* Vol. 18, Nov. 1975, pp. 1454-1459.

[7]Tidman, D. A., "Mega-Gauss Turbulence Due to Seeded Composition Fluctuations in Dense Plasma," *Physics of Fluids,* Vol. 19, Feb. 1976, pp. 321-326.

[8]Tidman, D. A., and Burton, L. L., "Magnetic Field Generation by Ablation Waves or Shocks Propagating in Inhomogeneous Plasma," *Physical Review Letters,* Vol. 37, No. 22, Nov. 1976, pp. 1397-1399.

[9]Stamper, J. A., Papadopoulos, K., Sudan, R. N., Dean, S. D., McLean, E. A., and Dawson, J. M., "Spontaneous Magnetic Fields in Laser-Produced Plasmas," *Physical Review Letters,* Vol. 26, No. 26, April 1971, pp. 1012-1015.

[10]Stamper, J. A., and Ripin, B. H., "Faraday-Rotation Measurements of Megagauss Magnetic Fields in Laser-Produced Plasmas," *Physical Review Letters,* Vol. 34, No. 20, Jan. 1975, pp. 138-141.

[11]Spitzer, Lyman, Jr., *Physics of Fully Ionized Gases,* 2nd ed., Wiley, New York, 1962, Chap. 2.

[12]Braginskii, V. I., "Transport Processes in a Plasma," *Reviews of Plasma Physics,* Vol. 1, edited by M. A. Leontovich, Consultants Bureau, New York, 1965, pp. 205-311.

[13]Landau, L. D., and Lifshitz, E. M., *Statistical Physics,* 3rd ed., Pergamon, Oxford, 1980, Sec. 104.

[14]Landau, L. D., and Lifshitz, E. M., *Electrodynamics of Continuous Media,* Pergamon Press, Oxford, 1960, p. 107.

[15]Landau, L. D., and Lifshitz, E. M., *Fluid Mechanics,* 2nd ed., Pergamon Press, Oxford, 1987, Sec. 89.

[16]Martin, J. J., *Atmospheric Re-entry,* Prentice-Hall, Englewood Cliffs, NJ, 1966, p. 238.

[17]Shercliff, J. A., *A Textbook of Magnetohydrodynamics,* Pergamon Press, Oxford, 1965, Sec. 7.9.

[18]Dresvin, S. V. (ed.), *Physics and Technology of Low Temperature Plasmas,* Iowa State Univ. Press, Ames, IA, 1977, Chap. 2.

[19]Liberman, M. A., and Velikovich, A. L., *Physics of Shock Waves in Gases and Plasmas,* Springer-Verlag, Berlin, 1986, p. 91.

[20]Gnoffo, P. A., "Aerothermodynamic Simulation Data," private communication.

[21]Canuto, C., Hussaini, M. Y., Quateroni, A., and Zang, T. A., *Spectral Methods in Fluid Dynamics,* Springer-Verlag, New York, 1987, pp. 204-207.

[22]Shebalin, J. V., "Broken Ergodicity and Coherent Structure in Homogeneous Turbulence," *Physica D,* Vol. 37, 1989, pp. 173-191.

[23]Murshed, H., private communication.

[24]Gazdag, J., "Time-Differencing Schemes and Transform Methods," *Journal of Computational Physics,* Vol. 20, 1976, pp. 196-207.

[25]Passot, T., and Pouquet, A., "Numerical Simulation of Compressible Homogeneous Flows in the Turbulent Regime," *Journal of Fluid Mechanics,* Vol. 181, 1987, pp. 441-466.

Henry B. Garrett
Associate Editor